Chapter 5
General Properties of the Terrestrial Planets

The terrestrial planets are confined to the inner solar system: Mercury, Venus, Earth (or Earth–Moon), and Mars. They differ from the main belt asteroids (Milone and Wilson 2014, Sect. 15.7.3) in being much more massive, and from the giant planets (Chap. 12) in being much less massive; they also lack the extensive mantles of hydrogen and helium of the gas giants. The rocky, central core of Jupiter is estimated to be between 10 and 20 Earth masses, and, if it became visible, might be considered the principal "terrestrial planet." However, the rocky cores of the outer planets are under greater pressures than are the interiors of the terrestrial planets,[1] and will have different traits. For example, they are expected to be mixed with large quantities of ices, and this is true also of the smaller bodies of the outer solar system. Thus the natures of the planets of the inner solar system are sufficiently unique to be discussed as a separate group, the "inner" or "terrestrial" planets.

5.1 Overview of Terrestrial Planets

The vast bulk of the rocky material of the terrestrial planets is hidden in the interior, so much of what we know about the material of each planet comes mainly from its bulk properties (i.e., the mean density, size, and mass) and the viewable surface. Although only the Moon and Earth have yielded sufficient material for detailed laboratory analyses, the surfaces of Mars and Venus have been examined by on-site probes and the composition has been investigated at a limited number of sites. Mercury is currently (2013) under intense scrutiny by the Messenger orbiter.

[1] Pressures of ~10^5 Pa (1 Pascal = 1 N/m^2 = 10^{-5} bar) for Earth's surface and ~3.64×10^{11} Pa for the Earth's core (Tromp 2001) compare to an estimated 4×10^{10} for the core of Mars (Stewart et al. 2007) and $>4 \times 10^{12}$ for that of Jupiter (Fortney 2007). The physical conditions in the rocky core of Jupiter are beyond current capability to recreate in the laboratory.

E.F. Milone and W.J.F. Wilson, *Solar System Astrophysics: Background Science and the Inner Solar System*, Astronomy and Astrophysics Library,
DOI 10.1007/978-1-4614-8848-4_5,

On the whole, the major and dwarf planets, and some of the major moons, are more spherical in shape than are most of the minor planets, moons, comets, and meteoroids that permeate the larger solar system, but none of them are precisely spherical. The approximate shape can be determined by direct filar micrometry (from ground-based telescopes) and, in most cases, those have been improved by direct imaging from space craft. The internal mass distributions can be and have been investigated by the perturbations on natural or artificial satellite orbits for all the planets.

The properties of planetary interiors have been investigated primarily through seismic effects (for the Earth and the Moon), magnetic field effects (for some), and the bulk properties such as radii, masses, mean densities, and surface densities (for all). In Chaps. 6 and 7, we deal with the properties of the interior and how they are known; the Moon will be treated separately in Chap. 8.

Telescopic observations of planets have been made since the early seventeenth century, and still continue to provide fresh insights and discoveries. The long history of observations of the once-alleged planet Vulcan, of Mercury and Venus rotation rates from perceived markings, and of putative Martian canals from perceived linear features demonstrates clearly that observations are not foolproof, but the discoveries of the lunar maria, the gibbous phases of Venus, Galilean satellites, the moons of Mars, the planet Uranus, the first asteroid, Ceres, and Charon (the moon of Pluto) changed our perception of the solar system in lasting ways. Ground-based telescopic observations still play a role today. A "great white spot" that suddenly appeared on Saturn and the signature of the first extrasolar planet in high-precision radial velocity measurements in the 1990s were such discoveries.

At the end of this chapter, we will touch on the visibility of planetary surfaces. We will define and discuss the significance of such terms as the *phase,* the *phase angle,* and *phase function* in studying the reflective properties of a solar system object. The surface features of the major terrestrial planets, namely Venus, Earth, and Mars, are quite similar in many respects, but there are also important differences among them, aside from the oceans of water on the Earth and the extensive atmosphere on Venus. In all the planets, impacts have played an important role in determining their physical and dynamical properties. These properties and the similarities and differences among terrestrial planets will be explored more thoroughly in Chap. 9.

Finally, the atmospheres and meteorology of the planets provide interesting differences in chemistry as well as physics. Atmospheric physics and atmospheric and ionospheric chemistry will be treated in detail in Milone and Wilson (2014, Chaps. 10 and 11).

5.2 Bulk Properties

The mean densities of the planets can be obtained simply from the bulk properties of mass and radius. The mass is directly obtained by observation of the semi-major axis of a moon in the case of most of the planets or from the acceleration of a space

probe in the case of Mercury, Venus, (most) asteroids, or comets. In either case, the acceleration of the smaller, less massive body is

$$\mathbf{a} = -\mu\,\hat{\mathbf{r}}\,/r^2 \tag{5.1}$$

where $\mu = GM$, and M is the planet's mass, r is the distance of the smaller body from the planet's center, and $\hat{\mathbf{r}}$ is a unit vector directed radially away from the planet's center. From (5.1), the magnitude of the acceleration at the surface of a planet of radius R is

$$\mathrm{a}\,(R) = g(R) = GM/R^2 \tag{5.1a}$$

Given M and R, the planet's mean density follows:

$$<\rho> \quad = \frac{M}{(4/3)\pi R^3} \tag{5.2}$$

The planet with the highest mean density is the Earth (5.515 g/cm^3 or 5,515 kg/m^3), that with the lowest, Saturn (690 kg/m^3). Because different types of material have different densities (e.g., liquid water, ~1,000 kg/m^3; the minerals pyroxene and olivine, ~3,300; iron sulfide, 4,800; and metallic iron, 7,900 kg/m^3), one might suppose that determining the composition would be a simple matter of getting the correct mixture of material. The volume fraction[2] $\mathrm{X_i}$ of material i contributes to the overall density through the relation:

$$<\rho> \quad = \quad \Sigma\,\rho_i X_i \tag{5.3a}$$

where $<\rho>$ is the mean density.[3] For instance, the planet Mercury has a mean density, $<\rho> = 5{,}430$ kg/m^3. We can predict the fraction of metallic iron, X_{Fe} and some average "rock," of density, say, $\rho = 3{,}500$, with a fraction $X_{\mathrm{rock}} = 1 - X_{\mathrm{Fe}}$. From (5.3a):

$$<\rho> \quad = \quad \rho_{\mathrm{Fe}} X_{\mathrm{Fe}} + \rho_{\mathrm{rock}}(1 - X_{\mathrm{Fe}}) \tag{5.4}$$

from which one may derive[4] $X_{\mathrm{Fe}} = 0.44$, and therefore, $X_{\mathrm{rock}} = 0.56$. But this can be misleading, because the mean density describes the bulk of material that is not at standard temperature and pressure (STP) conditions. Much of it is under extremely

[2] V_i/V_{total} where V is the volume and i a constituent.

[3] One may similarly compute the mass fraction (also referred to as X_i) from a relation of the kind,

$$1/<\rho> = \sum \{X_i/\rho_i\} \tag{5.3b}$$

[4] With the (compressed) mean density, one can derive a mass-fraction, $X_{\mathrm{Fe}} = 0.64$ for metallic iron, assuming that to be the only form that iron takes in Mercury.

Table 5.1 Planetary densities (kg/m^3)

Planet	ρ_{comp}	ρ_{uncomp}	Comments
Mercury	5,430	5,300	Still lots of iron!
Venus	5,240	4,000	
Earth	5,515	4,100	
(*Moon*	*3,360*	*3,300*	*Close to the density of Earth's mantle*)
Mars	3,940	3,700	

high pressure, and associated high temperature, so that the mean density, as determined from the mass and volume, has limited value in predicting the compositional mix. Models have, however, been constructed for planetary structure which permit estimates of the *uncompressed* density. See Table 5.1, taken from Consolmagno and Schaefer (1994, Table 4.2, Ch. 4.1, p. 71).

Notice that the Moon has the lowest mean density among these bodies and that its compressed and uncompressed densities are about the same. Note also the mild trend of lower uncompressed mean densities with increased distance from the Sun. Recalculating the volume and mass fractions with the *uncompressed* mean density of Mercury, the (assumed metallic) iron fractions become 0.41 and 0.61, respectively.

Another observable quantity involving bulk as well as dynamic properties is the *specific angular momentum* (SAM, the angular momentum per unit mass, **h**) of a planet and its satellites, because, as in the solar system generally, the distribution of angular momentum provides important clues to the origin of the planetary and satellite systems.

5.3 Gravitational Potential Fields

In this section we make use of conventional notation, which differs somewhat from that used in earlier chapters. If a planetary mass, M, is spherically symmetric, then a small mass, m, placed at a distance r from the centre of M has a *potential energy* (Fig. 5.1)

$$U = -\frac{GMm}{r} \tag{5.5}$$

The *gravitational potential*, V, is defined by the equivalence

$$\left\{\begin{array}{l}\text{gravitational}\\ \text{potential at } r\\ \text{due to } M\end{array}\right\} \equiv \left\{\begin{array}{l}\text{potential energy per unit}\\ \text{mass for mass } m \text{ located}\\ \text{at distance } r \text{ from } M\end{array}\right\}$$

That is,

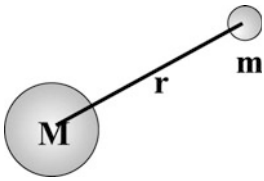

Fig. 5.1 Masses M and m have gravitational potentials and potential energies by virtue of their separation, r

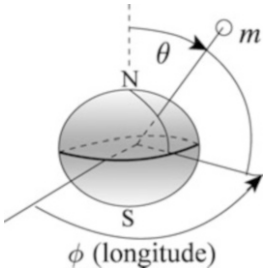

Fig. 5.2 Non-symmetric M

$$V \equiv \frac{U}{m} = \frac{\left[-\frac{GMm}{r}\right]}{m} = -\frac{GM}{r}, \tag{5.6}$$

Then, by way of a check, the potential energy of any mass m placed in this gravitational potential is:

$$U = mV = m\left(-\frac{GM}{r}\right) = -\frac{GMm}{r},$$

which agrees with (5.5).

If the mass M is *not* spherically symmetric, the strength and direction of the gravitational acceleration, **a**, are influenced by the actual distribution of mass inside M and by the location of m (in terms of r, θ, and ϕ) relative to the center of M, as shown in Fig. 5.2. Note the notation convention here, which differs from the usage of spherical astronomy in Chap. 2: the angle θ is called the *co-latitude* and is measured from the pole, not the equator. In the present context, the symbol ϕ is used for the longitude. V is now a function of r, θ and ϕ, and (5.6) no longer applies. It turns out that the equation for V can be written as a summation over an infinite series of spherical harmonics using *Legendre polynomials,* P_n (cos θ), and the *associated Legendre polynomials,* P_n^m(cos θ).

These are standard mathematical functions which are often encountered when using spherical coordinates. The properties of these polynomials are summarized in the addendum to this chapter (Sect. 5.6). With them, the potential in this spherical coordinate system can be written:

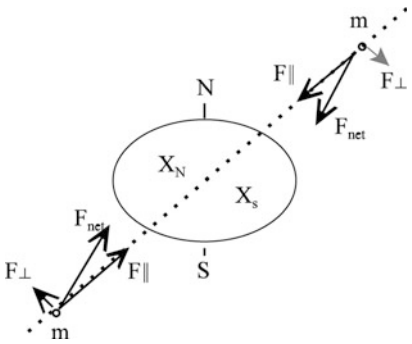

Fig. 5.3 Planet and satellite orbit plane

$$V = -\frac{GM}{r}\left[1 - \sum_{n=2}^{\infty}\left(\frac{a}{r}\right)^n J_n P_n(\cos\theta)\right] + \left[\sum_{n=2}^{\infty}\sum_{m=1}^{\infty}\left(\frac{a}{r}\right)^n (C_{nm}\cos\ m\phi + S_{nm}\sin\ m\phi) P_n^m(\cos\theta)\right] \tag{5.7}$$

where r is the distance and a is the mean radius of the planet. The polynomials are standard functions, so it follows that the coefficients must be determined by the particular mass distribution of any given planet. If we can find these coefficients from properties of the orbits of moons or of spacecraft, then (5.7) can, in principle, be "inverted" to find the mass distribution inside the planet required to produce these coefficients.

The terms in P_n do not involve the longitude, ϕ, and so describe mass distributions that are symmetric about the rotation axis but vary with latitude (as, for example, in a rotationally flattened sphere). The terms in P_n^m do involve ϕ and so describe the amount of departure from axial symmetry (longitude-dependent mass distributions).

Even-numbered J_n (J_2, J_4, ...) describes mass distributions that are symmetric about the equatorial plane (the northern hemisphere is a mirror image of the southern hemisphere), whereas odd-numbered J_n (J_1, J_3, ...) describes asymmetric distributions (such as a pear shape, for example). J_1 is missing (i.e., $n = 1$ is missing from the summation) because $n = 1$ corresponds to a bodily movement of the sphere in some direction away from the center of the coordinate system. For simplicity, we define our coordinate system to be centered on the center of the sphere, so J_1 disappears. J_2, the coefficient for the second spherical harmonic term, is called the *quadrupole moment* and measures the amount of polar flattening. It is generally the simplest to find. Figure 5.3 shows a satellite (either natural or artificial) in an inclined orbit around a planet which is rotationally flattened.

If there are no other "irregularities" in the planet, then rotation produces a mass distribution which is symmetric about the equator. The plane of the satellite's orbit "slices" the planet into two halves of equal mass, as shown in Fig. 5.3, where the dotted line marks the plane of the orbit of the small body of mass m and

where X_N and X_S mark the centers of mass of the northern and southern portions of the planet delineated by the plane of the orbit. When the satellite is north of the planet's equator, it is closer to the center of mass of the southern half of the planet X_S than to that of the northern half, X_N, as shown, and so feels a net off-center pull toward the south. This force can be resolved into two components, one in the plane of the orbit (toward the planet's center) and one at right angles to the orbit. The force toward the center is the centripetal force, the geometric description of the gravitational force of the planet that keeps the satellite in orbit, while the force at right angles in effect creates a torque on the orbit. As with a simple gyroscope spinning on one end on a desk, this gravitational torque causes the orbit to precess. The rate of precession depends on the amount by which the center of mass of each half of the planet is offset from the planet's center, and therefore the precession rate also depends on the amount of flattening and on the mass distribution inside the planet (the same amount of flattening will produce less offset in a planet with mass more concentrated toward the center).

J_2 can be calculated from the rate of precession and provides an important tool for probing the interior of a planet.

The higher-order terms and longitude-dependent terms are due to departures from the simple rotational flattening described above and give a measure of the extent to which non-hydrostatic forces (i.e., other than gravity and rotation; for example, rising mantle plumes, mountain-building due to lithospheric convergence, massive lava flows supported by stresses in the planet, etc.) have affected the mass distribution in the planet. They show up observationally as changes in the plane, orientation, size, eccentricity, and period of the satellite's orbit.

Two other useful sets of numbers, h_n and k_n ($n \geq 2$), were developed by A. E. H. Love (1911) to describe tidal effects (see Sect. 3.7). Specifically, h_2 describes the ratio of the height of the solid-body tide to the height of the static equilibrium tide (an idealized oceanic tide in which the water achieves static equilibrium with the tidal forces, forming a prolate spheroid with its long axis in line with the perturbing body), and the *potential Love number* k_2 describes the ratio of the gravitational potential of the perturbed (tidally-deformed) body at a point to the perturbing potential at that point. Here, we are concerned with k_2.

Consider an initially-spherical satellite of radius R whose distance, d, from a planet of mass M is small enough that the satellite is tidally distorted by the planet, but large enough that the planet can be treated as a point mass, as illustrated in Fig. 5.4. The planet-satellite scenario is used here for convenience of terminology, but the arguments apply equally well to any two bodies that satisfy the conditions in the previous sentence; e.g., a planet tidally-distorted by its satellite, a planet orbiting the Sun or another star, or a planet being perturbed by another planet.

The gravitational potential, $\Phi(\vec{r})$, at any point Q located at a displacement $\vec{r}$ from the center, C, of the satellite in Fig. 5.4 can be written as

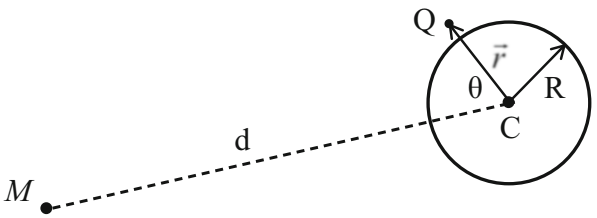

Fig. 5.4 A figure for defining the potential Love numbers

$$\Phi(\vec{r}) = W(\vec{r}) + V(\vec{r}) \tag{5.8}$$

where $W(\vec{r})$ is the potential at Q due to the planet and $V(\vec{r})$ is the potential at Q due to the satellite. If a spacecraft or other object passes the satellite, then $W(\vec{r})$ determines the path that the spacecraft would follow if the satellite were not there, and $V(\vec{r})$ determines how this path is perturbed by the presence of the satellite.

$W(\vec{r})$ can be expanded in a harmonic series using the Legendre polynomials defined above:

$$W(\vec{r}) = -\frac{GM}{d}\sum_{n=0}^{\infty}\left(\frac{r}{d}\right)^n P_n(\cos\theta) \equiv \sum_{n=0}^{\infty} W_n \tag{5.9}$$

It is instructive to examine the first three terms of (5.9):

$$\begin{aligned} W(\vec{r}) &= -\frac{GM}{d}\left(\frac{r}{d}\right)^0 P_0(\cos\theta) - \frac{GM}{d}\left(\frac{r}{d}\right)^1 P_1(\cos\theta) - \frac{GM}{d}\left(\frac{r}{d}\right)^2 P_2(\cos\theta) - \ldots \\ &= -\frac{GM}{d}(1)(1) - \frac{GM}{d^2} r\cos\theta - \frac{GM}{d^3} r^2 \frac{1}{2}(3\cos^2\theta - 1) - \ldots \end{aligned} \tag{5.10}$$

The n = 0 term is the gravitational potential due to the planet at the center of the satellite, the n = 1 term is related to the gravitational acceleration due to the planet at the center of the satellite, and, from (3.55), the n = 2 term is related to the tidal force per unit mass on the satellite by the planet. The *tide-raising potential* is thus given by the sum of terms $n \geq 2$ in (5.9). Because of the factor $(r/d)^n$ in (5.9), if $r << d$ then terms $n > 2$ (i.e., terms beyond those shown in (5.10)) can often be neglected.

We note here that the n = 1 term in (5.9) and (5.10) is present because the origin of the coordinate system is at the center of the satellite and not at the center of the gravitating body (the planet); compare this with (5.7), where the n = 1 term is absent (the summation begins at n = 2) because the coordinate system is centered on the gravitating body.

$V(\vec{r})$ can in principle be found by adding up (i.e., integrating) the potentials at Q due to all the mass elements, dM, within the satellite:

$$V(\vec{r}) = -G\int \frac{dM}{\left|\vec{r} - \vec{r}'\right|} = -G\int \frac{\rho(\vec{r}')}{\left|\vec{r} - \vec{r}'\right|} \mathrm{dv}' \tag{5.11}$$

where $\rho(\vec{r}')$ is the density at any point $\vec{r}'$ within the satellite, and dv′ is the volume element at point $\vec{r}'$. $V(\vec{r})$ thus depends on the density distribution within the satellite. In practice, the density distribution within the satellite is unknown, and we would like to learn something about it by evaluating the tidal terms in (5.9).

The potential at Q due to the satellite can be described by a harmonic series of the same form as (5.9). Love (1911, p. 53) showed that the tidally-induced potential V_2 at r can be represented by a function K(r) times the tide-raising potential, W_2, from (5.9). Then, neglecting terms n > 2,

$$V = V_0 + V_2 = V_0 + K(r)\, W_2 \tag{5.12}$$

where V_0 is the potential at r of the undistorted (spherical) satellite, the (missing) second term from (5.9) is zero because the coordinate system is centered on the gravitating body for potential V (the satellite), and the function K(r) is constant over a surface of a given r.

The potential Love number k_2 is defined from (5.12) as the ratio of the tidally-induced potential to the tidal potential, both evaluated at the mean radius, R, of the satellite; i.e., $k_2 \equiv K(r = R)$:

$$k_2 \equiv \frac{V_2(r = R)}{W_2(r = R)} \tag{5.13}$$

(If terms n > 2 are retained then there are also higher-order potential Love numbers, k_n.)

For a uniform satellite, k_2 is related to the *effective rigidity*,

$$\widetilde{\mu} = \frac{19\mu}{2\rho g R} \tag{5.14}$$

of the satellite by

$$k_2 = \frac{3}{2}\left(\frac{1}{1 + \widetilde{\mu}}\right) \tag{5.15}$$

(Love 1911, p. 62; see also Henning et al. 2009). Here, μ is the rigidity of the material, ρ is the density, and g is the gravitational acceleration at the surface of

the satellite (r = R). The quantity μ is discussed again in Sects. 5.4.1 and 5.4.2. The effective rigidity, $\widetilde{\mu}$, is a dimensionless ratio that compares the elastic forces in the numerator to the gravitational forces in the denominator (Henning et al. 2009); i.e., $\widetilde{\mu}$ is a measure of how effective the rigidity is at preventing the body from reaching hydrostatic equilibrium by self-gravitation. The product $\rho g R$ can be thought of as a "gravitational stiffness" analogous to the rigidity. If $\widetilde{\mu} >> 1$ the satellite is dominated by its rigidity and if $\widetilde{\mu} << 1$ it behaves like a self-gravitating fluid.

From (5.15), k_2 can range from 0 for $\widetilde{\mu} = \infty$ to 1.5 for $\widetilde{\mu} = 0$. The former applies to a completely rigid satellite [this can also be seen from (5.13): if the satellite remains tidally undistorted, then $V_2 = 0$] and the latter to an incompressible fluid body. A satellite with a fluid layer, as, for example, a subsurface ocean, would typically have a value of k_2 near 0.4. Thus, although (5.11) cannot be inverted to find the density distribution once k_2 is known, the value of k_2 does provide useful constraints on interior models of satellites orbiting planets, or planets orbiting stars.

In practice, k_2 is generally determined from the motion of a spacecraft as it passes by or is in orbit around the satellite.

5.4 Structure of the Earth

Through the physics of wave phenomena, the structure of the interiors can be explored. The type and amount of refraction of waves are the means of exploration. Seismic events can be either natural ("quakes") or artificial, i.e., an explosive charge can be set off at some site and the response as a function of distance from that site can be recorded by seismometers set up in a net around the site. In particular, changes in wave velocity show up in a distribution of travel times with distance. The delay time as a function of position along the surface can be modeled by gradual and sharp changes of velocity in the interior and can reveal the presence of discontinuities in the refractive properties of the interior layers.

5.4.1 Seismic Studies

Seismic studies are most mature for the Earth, but the Moon has an array of seismic detectors on its surface which were placed there by the Apollo astronauts between 1969 and 1972. Thus far there have been no comparable studies of Venus and Mars. On Venus, Veneras 13 and 14 carried seismometers that returned data during the 1–2 h that each lander operated on the surface. No events were detected by Venera 13, and Venera 14 detected two possible microseismic events from sources estimated to be within 3,000 km of the lander (Ksanfomaliti et al. 1982); however, while considered less likely, an origin in wind gusts or other local phenomena could not be entirely ruled out. The only seismometers placed on Mars were on the Viking 1 and 2 landers, but the one on Viking 1 did not deploy properly and was unable to return

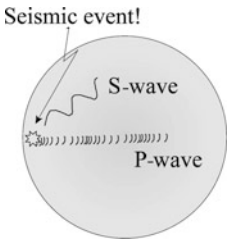

Fig. 5.5 P- and S-waves

data. The Viking 2 seismometer operated for 500 Martian days, during which one candidate local seismic event was identified (Lorenz and Nakamura 2013). No future lander missions have been announced for Venus, although Hunter et al. (2012) have developed a high-temperature seismometer for use on Venus should such a mission occur. NASA's InSight lander mission to Mars, currently scheduled for launch in 2016, will carry a seismometer and other geophysical instrumentation. It was originally hoped that ESA's ExoMars mission would include a seismometer, but this and several other instruments were cancelled in the final design selection.

Seismic events such as earthquakes release energy that displaces and distorts rock at considerable distances primarily through two types of waves: *P-waves* and *S-waves,* illustrated in Fig. 5.5.

P or *primary* waves are also known as pressure waves, push-pull waves, longitudinal waves, and compressional waves. They are analogous to sound waves.

S or *secondary* waves are also known as shear waves, shake waves, and transverse waves. These are analogous to light or, more generally, electromagnetic waves.

P- and S-waves are *body waves* (through the Earth). *Surface waves* are also produced: L-waves and Rayleigh-waves, analogous to water waves and ripples, respectively. These diminish rapidly below the surface.

When waves are generated by an earthquake, the P-waves travel faster than the S-waves and arrive first at any given location. The speed of a wave depends on:

1. The type of wave (P or S)
2. The density of the medium
3. The state of the material (solid, liquid, or gas)
4. The composition (granite, basalt, iron, . . .)
5. The mineral phase (e.g., the wave speed is different in graphite and diamond, even though they are both forms of carbon)
6. The compressibility, K, for P-waves, and the rigidity, μ, for P- and S-waves. K and μ depend on the density, and the density, in turn, depends on the composition and the mineral phase (as well as the temperature and the pressure), so in fact the wave speed depends very strongly on the density

Because pressure ("P") and shear ("S") waves differ in their speeds through material (e.g., the S-waves do not propagate through fluids), the physical state of the material can be found. Thus the Earth has an outer core that is liquid, revealed by a "shadow zone" in which the S-waves are not seen on the surface. The structure of the interior is then deduced through the solution of equations describing the

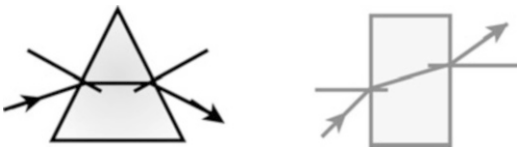

Fig. 5.6 Snell's law

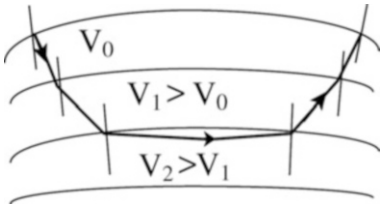

Fig. 5.7 Constant v in each layer

expected physics of the interior: an equation of state, which relates the density, pressure, mean molecular weight, and temperature; an equilibrium equation that relates the pressure with the weight per unit area; expressions of the conservation of mass; and an expression which describes heat flow.

The travel paths of seismic waves are decided by the refraction properties of the medium. Snell's law applies:

$$n_1 \sin\theta_1 = n_2 \sin\theta_2 \tag{5.16}$$

where the index of refraction, n, depends on the speed of the wave.

As Fig. 5.6 demonstrates, a wave is bent *toward* the normal if it travels from a region of lower refractive index to a region of higher refractive index (i.e., higher wave speed to lower wave speed), because $n_2 > n_1 \Rightarrow \theta_2 < \theta_1$. It is bent *away from* the normal if it travels from a region of higher refractive index to a region of lower refractive index (corresponding to a region with lower wave speed to one of higher wave speed), because

$$n_1 > n_2 \quad \Rightarrow \quad \theta_2 > \theta_1.$$

The path in a layered sphere involves additional considerations. Density generally increases with depth into the Earth so, except at certain discontinuities, the wave speed, v, increases with depth. The refractive index thus generally decreases with depth. We consider five conditions:

1. A layered sphere, v constant in each layer (Fig. 5.7): the ray refracts *away* from the normal going in and *toward* the normal going out.
2. A sphere in which v increases smoothly with depth (Fig. 5.8): this is the same as if the layers were infinitesimally thin. The refraction then becomes continuous.
3. A seismic discontinuity at which v suddenly decreases and afterward continues to increase (Fig. 5.9): the refractive index suddenly increases, so the wave refracts toward the normal.

   Also, both reflection and refraction take place at any boundary.

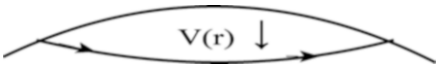

Fig. 5.8 *v* increasing smoothly with depth

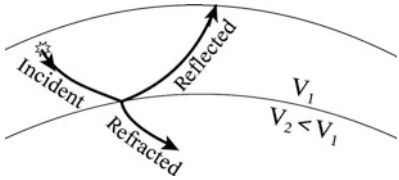

Fig. 5.9 *v* increase discontinuous

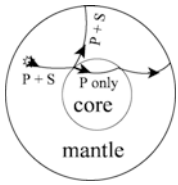

Fig. 5.10 Liquid layer passes only P-waves

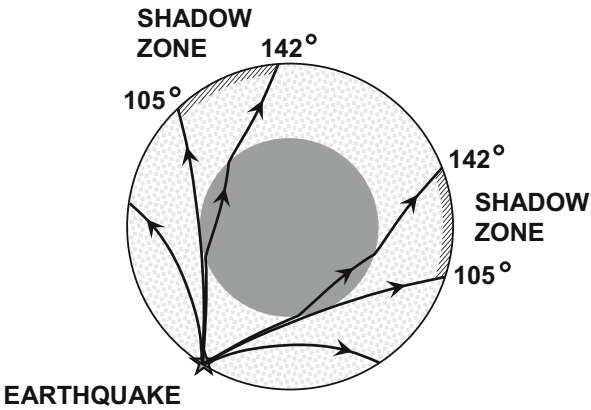

Fig. 5.11 $v_{\text{liq core}} << v_{\text{mantle}}$. Waves that just miss the core boundary return to the surface 105° from the earthquake, whereas those that just contact the core boundary refract into the core and out again, and return to the surface 142° from the earthquake. Between the two is a shadow zone in which no direct P waves are seen

4. Liquid layer: S-waves cannot propagate unless there is a restoring force in the transverse direction. No such force exists in a liquid (a liquid has no "rigidity"), so S-waves cannot propagate in a liquid. No S-waves are observed to travel through the outer core, so the outer core is known to be liquid.

   It appears to be molten iron (Fig. 5.10).
5. Shadow zone (see Figs. 5.11 and 5.12): The speed of P-waves in the liquid outer core of the Earth is much less than in the mantle just above it (13 km/s in the mantle, 8 km/s in the core); *v* thus decreases suddenly at the core–mantle boundary.

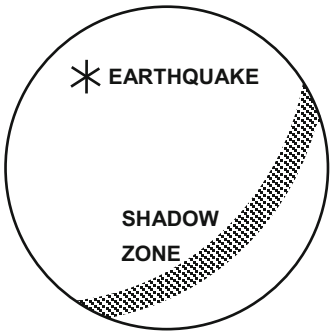

Fig. 5.12 No seismic waves in shadow zone

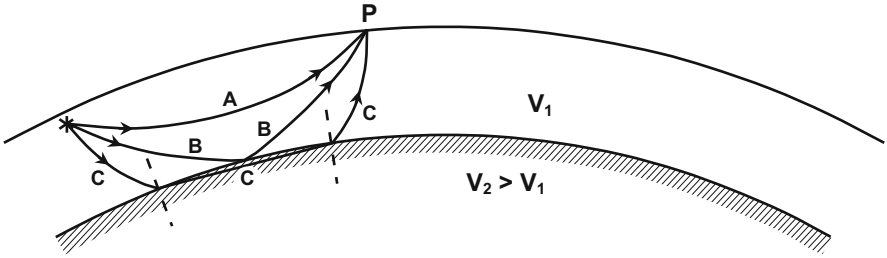

Fig. 5.13 Three wave paths from earthquake site to Station P

As shown in Figs. 5.11 and 5.12, refraction at the core-mantle boundary creates a shadow zone where no seismic waves will be received. (Body waves may reach there by other processes, such as reflection from the inner core, but these are much weaker than the "direct" P-waves so the shadow zone is still easily observable.) The speed of the wave determines its behavior, so the time intervals for the wave to reach various locations from the site of origin provide the data for modeling the refractive properties of the layers through which it passes.

If there is a seismic discontinuity in which v increases suddenly at some depth, then a station located within a certain range of distances from an earthquake can receive waves by three different travel paths (Fig. 5.13):

Speed increases smoothly with depth until the discontinuity is reached, so the station receives waves as follows.

A. Seismic wave takes the most direct path. This has the slowest average v but the shortest path; it arrives first.
B. Seismic wave reflects from the discontinuity. It has faster average speed (travels deeper) but along a longer path; it arrives later than A.
C. The wave refracts into the faster layer, then out again. It has a longer path than B, but the higher speed in the lower layer more than compensates for the longer path; it arrives before B, but after A. The arrival times at station P are plotted in Fig. 5.14.

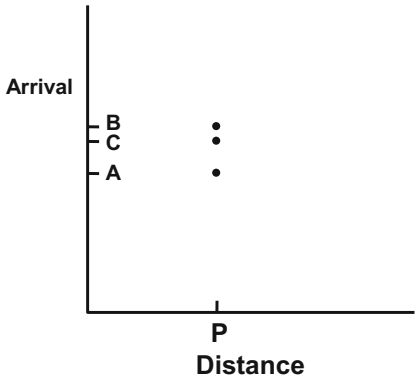

Fig. 5.14 Arrival times of seismic waves at station P

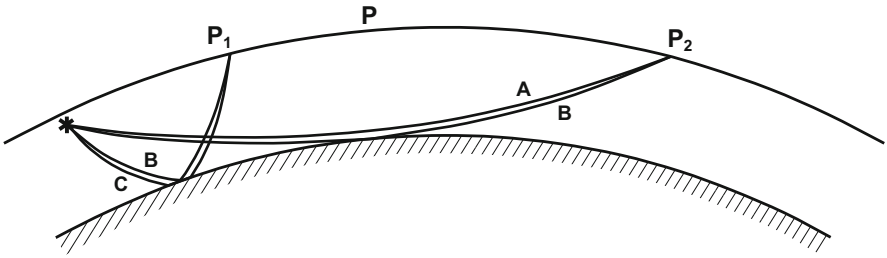

Fig. 5.15 Moving station P change the travel times

If we move P closer to the earthquake site, then the travel path of wave C in the lower layer decreases, eventually becoming zero at point P_1 in Fig. 5.15. The travel times for waves B and C thus approach each other, becoming equal at P_1 .

If we move P further from the earthquake, then the lengths and travel times for paths A and B approach each other, becoming equal at point P_2 in Fig. 5.15.

If we plot the arrival times of waves observed at various stations as a function of the distance of each station from the epicenter of the earthquake (the point on the surface of the Earth directly above the earthquake), then we find the arrival time plot as shown in Fig. 5.16

Plots such as these can be used to find wave speed as a function of depth into the Earth.

An example of seismic waves arriving at stations in Alberta, Canada, from the Fukushima, Japan, earthquake of March 11, 2011, is shown in Fig. 5.17. This earthquake measured magnitude 8.9 on the Richter scale (Richter 1935; Gutenberg and Richter 1936).

5.4.2 The Adams–Williamson Equation

A derivative expression, the Adams–Williamson equation, relates the velocities of the P and S-waves deduced from the seismic models to the density gradient, $d\rho/dr$,

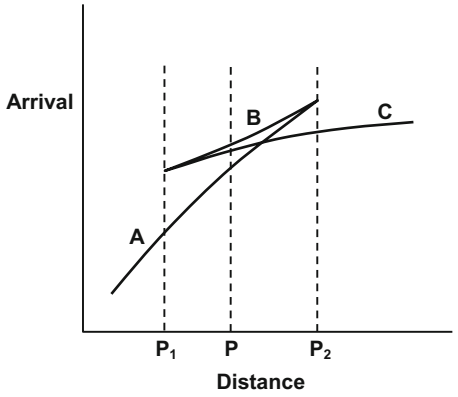

Fig. 5.16 Arrival time of S-waves as a function of the distance of the observing station from the earthquake, measured along the surface of the Earth. The data are from a simplified two-layer model of the outer mantle with a seismic discontinuity 670 km below the surface, and S-wave speeds 4.0 km/s above the discontinuity and 6.0 km/s below

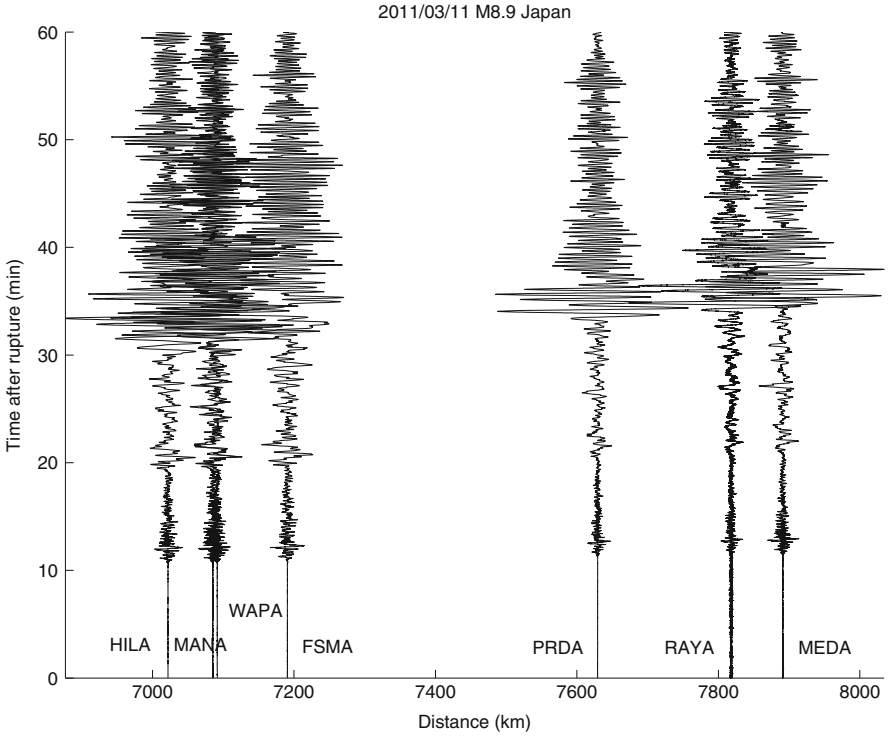

Fig. 5.17 Seismograms of the magnitude 8.9 earthquake in Fukushima, Japan, on March 11, 2011, recorded at seven seismograph stations in Alberta, Canada. The x-axis shows distance from the epicenter. Time increases upward. The initial, lower-amplitude, part of each waveform represents body (P and S) waves that have travelled on shorter paths through the mantle. Of these, the P waves arrive first, followed by the S waves. The later, high-amplitude waves that arrive 30 s or more after rupture are surface waves that have travelled close to the Earth's surface from the earthquake to the seismometer station. FSMA = Fort Smith, HILA = High Level, MANA = Manning, MEDA = Medicine Hat, PRDA = Rothney Astrophysical Observatory near Priddis, RAYA = Raymond, WAPA = Wapiti River. Courtesy, Dr. David Eaton, University of Calgary Dept. of Geoscience

at a distance r from the center. The usual procedure is to consider the interior to be a series of shells of thickness dr and to express the change in density, $d\rho$, across that shell. The density depends also on the molecular weight of the material in the interior, and this is not known exactly. However, it can be guessed. The Adams-Williamson equation is derived as follows:

Start with the equation of hydrostatic equilibrium (the derivation of which is one of your end-of-chapter Challenges!):

$$\frac{dP}{dr} = -\rho g = -\frac{GM(r)}{r^2}\rho \tag{5.17}$$

where $M(r)$ is the mass enclosed within radius r.

Define the *bulk modulus*, k, through the relation

$$\frac{d\rho}{dP} = \frac{\rho}{k} \tag{5.18}$$

Rewriting (5.18), substituting from (5.17), and dividing top and bottom of the right-hand side by ρ, we get:

$$\frac{d\rho}{dr} = \frac{d\rho}{dP}\frac{dP}{dr} = \frac{\rho}{k}\frac{dP}{dr} = -\frac{GM(r)\rho}{\frac{k}{\rho}r^2} \tag{5.19}$$

Then, making use of the relations between these quantities and the primary and secondary wave speeds,

$$v_p^2 = \frac{m}{\rho} = \frac{k + \frac{4}{3}\mu}{\rho}, \quad v_s^2 = \frac{\mu}{\rho} \tag{5.20}$$

where m is the *elastic modulus* and μ is the *rigidity* or *shear modulus*,[5] so that, combining the (5.20) expressions,

$$v_p^2 = \frac{k}{\rho} + \frac{4}{3}v_s^2 \tag{5.21}$$

and, rearranging (5.21),

$$\frac{k}{\rho} = v_p^2 - \frac{4}{3}v_s^2 \tag{5.22}$$

[5] For the derivation of these quantities in terms of stresses and Young's modulus, see, for example, Stacey (1969), pp. 85–86.

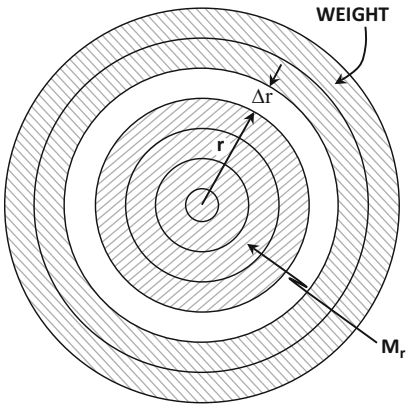

Fig. 5.18 Shells for numerical integration of (5.25)

we arrive at what has been called the "fundamental equation of geology," the *Adams–Williamson* equation:

$$\frac{\mathrm{d}\rho}{\mathrm{d}r} = -\frac{GM(r)\rho}{r^2\left(v_p^2 - \frac{4}{3}v_s^2\right)} \tag{5.23}$$

Now we go on to discuss how to solve this equation in order to find the density, ρ, as a function of r inside the Earth.

Equation (5.23) tells us the change (dρ) in ρ over some small distance dr:

$$\frac{\mathrm{d}\rho}{\mathrm{d}r} = f \qquad \Rightarrow \qquad \mathrm{d}\rho = f\,\mathrm{d}r \tag{5.24}$$

where f represents the right-hand side of (5.23). Then to find ρ as a function of r, we need to integrate (5.24).

$$\rho = \int \mathrm{d}\rho = \int f\,\mathrm{d}r. \tag{5.25}$$

This involves numerical integration; we describe the procedure in a step-wise manner:

First, divide the Earth into many thin shells, as shown in Figs. 5.18 and 5.19.

Each shell has uniform composition and density.

Then the density, ρ, in each shell depends on:

1. mineral composition;
2. compression of the shell by the weight of all the shells above it.

Decide on a model for the Earth's composition as a function of r, for example: olivine/pyroxene mantle, iron core.

Note that we can express the total mass, M_r, interior to any radius, r, either by:

$$M_r = \int_{a=0}^{r} \mathrm{d}m = \int_{a=0}^{r} \rho(a)\,\mathrm{d}V = \int_{a=0}^{r} \rho(a)\,4\pi a^2\ \mathrm{da} \tag{5.26}$$

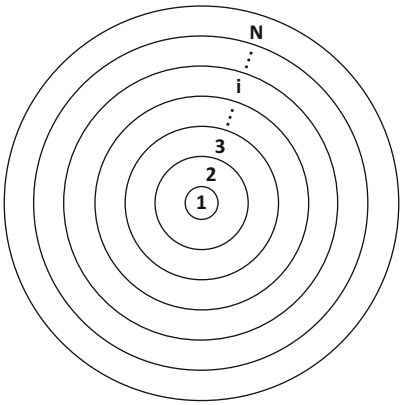

Fig. 5.19 Setting up *N* Shells

or by

$$M_r = M_E - \int_{a=r}^{R_E} \mathrm{d}m = M_E - \int_{a=r}^{R_E} \rho(a)\, 4\pi a^2 \ \mathrm{da} \tag{5.27}$$

where M_E and R_E are the Earth's mass and radius respectively. Equation (5.27) is more useful than (5.26), because it involves only quantities above the radius r, and these are known at any given r, as described below.

As we are going to integrate numerically, we need numbers, and an infinitesimal quantity like da or dr is not a number. Therefore, we need to convert (5.23) and (5.27) to *finite difference equations*, the mathematical equivalent of "going digital."

Taking (5.27) first, we replace da by the width, Δr_i, of the i$^{\text{th}}$ shell:

$$M_r = M_E - \sum \rho_i 4\pi r_i^2 \ \Delta r_i \tag{5.28}$$

We know M_E and R_E, and we know ρ at the surface of the Earth. Now we can go through an iterative loop, working inwards from the Earth's surface.

LOOP:

1. Decide on a thickness Δr_i for this shell.
2. Use (5.28) to calculate M_r (Note: the RHS is known). This involves numerical integration.
3. Rewrite the Adams–Williamson equation as a finite difference equation:

$$\Delta\rho_i = \left\{ \frac{GM_r\rho_i}{r_i^2\left[(v_P)_i^2 - \frac{4}{3}(v_S)_i^2\right]} \right\} \Delta r_i \tag{5.29}$$

where M_r was found above, and v_P and v_S are known from the seismic data.

This gives $\Delta\rho_i$, the change in ρ across the shell, so ρ for the next shell inward is:

$$\rho_{i-1} = \rho_i + \Delta\rho_i. \tag{5.30}$$

We continue looping until we either run out of mass ($M_r = 0$) or run out of radius ($r_i = 0$). Because M_r has to be 0 exactly at $r = 0$, we have to adjust the composition and other input assumptions until they both go to zero at the same time. We now have the density, ρ, as a function of r. The model also has to allow for mineral phase changes, e.g., the crystal structure of olivine changes at about 150–200 kbar pressure to a new crystal structure; it is then called *spinel* and is about 10 % denser than the original crystal structure (*olivine*) at the same pressure. See Chap. 7 for a discussion of mineral structure.

5.4.3 Moments of Inertia

The moment of inertia I, of the Earth depends on the distribution of mass (and therefore density) inside the Earth:

$$I = \sum m_i r_i^2 \tag{5.31}$$

For a uniform sphere of radius R and mass M, one may show that

$$I = (2/5)\ MR^2 \tag{5.32}$$

In general, however,

$$I = KMR^2 \tag{5.33}$$

See Fig. 5.20 for the effect of different density distributions on K. Note that I is lower if most of the mass is close to the center (in the core) and I is higher if most of the mass is further out (in the mantle). We can calculate the moment of inertia for our model of density as a function of radius and compare that to the observed value. If the two are different then we can adjust our model to bring it into agreement with the observations.

With regard to orbiting satellite observations, we note that the second harmonic can be written in terms of the moments of inertia:

$$J_2 = \left[I_z - I_{x,y}\right] / \left(Mr^2\right) \tag{5.34}$$

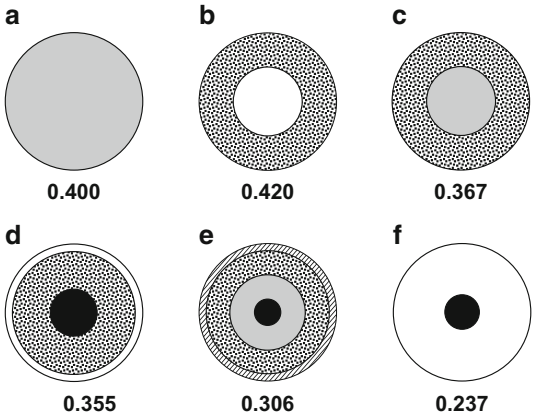

Fig. 5.20 The effect of density distribution on K. Outer radius, 1 unit. (**a**) *Undifferentiated asteroid or comet*. Uniform density. (**b**) *Density inversion*. Core: $r = 0.5$, $\rho = 0.5$; mantle: $\rho = 1.00$. (**c**) Core: $r = 0.5$, $\rho = 2.00$; mantle: $\rho = 1.00$. (**d**) *Callisto model*. Core: $r = 0.34$, $\rho = 3.5$; mantle: $r = 0.89$, $\rho = 2.1$; crust: $= 1.0$. (**e**) *Terrestrial planet model*. Inner core: $r = 0.19$, $\rho = 12.8$; outer core: $r = 0.55$, $\rho = 11.2$; lower mantle: r = 0.895, $\rho = 4.9$; upper mantle: $\rho = 3.6$. (**f**) *Jovian planet model*. Core: $r = 0.25$, $\rho = 20$; mantle: $\rho = 0.4$. (Densities in g/cm^3.)

where I_z is the moment of inertia about the rotation axis of the planet and $I_{x,y}$ is the moment of inertia about an axis in the equatorial plane. Two effects of J_2 on the orbit (see Sect. 3.2 of Chap. 3 for definitions) are:

$$\mathrm{d}\omega/\mathrm{d}t = -\ (3/2)J_2\left(n/p^2\right)\left[(5/2)\ \sin^3 i - 2\right] \tag{5.35}$$

the change in the argument of pericenter, where $p = \mathrm{a}(1 - \mathrm{e}^2)$, and

$$\mathrm{d}\Omega/\mathrm{d}t = -\ (3/2)J_2\left(n/p^2\right)\ \cos i \tag{5.36}$$

the change in the longitude of the ascending node. An effect on the mean motion, and thus the position of the object in its orbit, is:

$$[t - T_0]\,\mathrm{d}n/\mathrm{d}t = -(3/2)J_2\left(n/p^2\right)\left[(5/2)\ \sin^3 i - 2\right] \tag{5.37}$$

5.4.4 Models of the Interior

Knowledge of the Earth's interior can be obtained, with varying degrees of certainty, from seismology, geomagnetism, geochemistry, high-pressure experiments, and samples of crustal material. To some extent, the mantle can even be sampled directly: some upper mantle material reaches the surface in mid-ocean ridge lavas, and some lower-mantle material is believed to become entrained in deep mantle

plumes and reaches the surface in some ocean island basalts (hot-spot volcanism) (Deschamps et al 2011). Cosmically, a rare class of carbonaceous meteorite, the CI chondrites [five examples known from falls; a few more are known from finds in Antarctica (Islam et al. 2012)], have almost exactly solar abundances of the elements, with the exception of hydrogen and helium. They are therefore believed to be remnants of the original protoplanetary disk (i.e., they are the most primitive meteorites), and provide a reference for studying processes in the Earth that have altered these abundances. For example, assuming a bulk CI chondritic composition for the Earth, *lithophile* ("rock-loving") elements that are over-abundant in the mantle would be so because they were excluded from the core, and *siderophile* ("iron-loving") elements that are depleted in the mantle would be so because they were preferentially carried into the core. Iron, stony-iron and some stony meteorites also provide information about *differentiation*, the separation of planetary and asteroidal bodies into crust, mantle and core. Knowledge of the present state of the Earth's interior then provides a basis for modeling the formation and evolution of the Earth. For a comprehensive discussion of these meteorites, see Chap. 15 in Milone and Wilson (2014), for chondrites in particular, Sects. 15.1.3.1 and 15.2, and for CI especially, 15.2.2.

On the computational side, numerical integration of the Adams–Williamson equation produces a march of the density, ρ, with distance from the center (Sect. 5.4.2). The models are constrained by the surface boundary layer where the density, pressure, and temperature drop sharply, and by the bulk properties of the planet: the mean density and radius. Once $\rho(r)$ is known, equations of state (equations relating T and P to ρ) can be used to find T and P as functions of r. Examples of models may be seen in Figs. 5.24, 5.25, and 5.26 and 6.12. In these models, density, temperature and pressure are all seen to increase inward through the interior.

Radioactive dating of meteorite samples has provided an age for the solar system of 4.568×10^9 year (Wood 2011). This is the time at which dust in the solar nebula began to accrete to form the planets, asteroids and comets. The first small objects formed by dust grains clumping together, and as objects became more massive, collisions resulting from mutual gravitational perturbations became more important. By ~10^4–10^5 years, when many objects were in the 10-km size range, gravitational perturbations dominated the accretion process, and by ~10^6 years a few tens of objects had grown into planetary embryos of a few per cent the mass of the Earth.

The growth of the terrestrial planets appears to have followed an approximately exponential law, $M(t) = M_{final}(1 - e^{-t/\tau})$, with a time constant, τ, in the case of the Earth of approximately 10 or 11 million years (Wood 2011). Thus, growth was most rapid at the start, 95 % complete at $t = 3\tau$, and 98 % complete at 4τ (~40 Ma for the Earth).

The Earth's core (discussed in detail below) is expected to contain primarily iron with substantial amounts of nickel, mixed with sulfur, oxygen, and other elements. The mantle and crust of the Earth, on the other hand, are much richer in silicates. With an assumption about the density at the center ($r = 0$), the differences in density can be added, shell by shell, to determine the interior density at every radius from the center. In this way, the interior structure can be induced. Thus the

core takes up the inner 3,500 km from the center (the outer 2/3 of which appears to be liquid), the mantle approximately 2,900 km, and the crust a mere 50–100 km. The mantle itself has structure: in the upper mantle, a deeper, more fluid component (the *asthenosphere*) underlies the solid *lithosphere,* which includes the crust.

The lithosphere "rides" on the asthenosphere in the form of "plates" driven by convective regions in the asthenosphere. The effect is to produce regions of *orogenesis,* or mountain-building, and *subduction,* regions where one plate (e.g., an oceanic plate) flows below another (typically a continental plate). The result is continental drift, in which continents move at rates of the order of 1 cm/year, and where areas which are subducted are replaced by new influx of material along mid-oceanic rises, producing seafloor spreading. The vent areas are outgassing, warm, and rich in sulphur and other material, and it is suspected that life began on the Earth in just such areas; in any case, there is a variety of living organisms currently found at such sites. The temperature of the lava that spreads out away from the upwelling areas rapidly falls below the *Curie point*, so the ferro-magnetic material in it aligns with the local magnetic field in effect at the time and remains that way. Thus, the magnetic reversals in the Earth's field can be studied in the remanant magnetism trapped in successive bands of cooled lava oriented parallel to the mid-ocean ridge as the ocean floor spreads away from the ridge.

The major arguments supporting iron as the dominant component of the Earth's core are,

1. Density models derived from seismic data and the Adams-Williamson equation (and therefore independent of assumptions about composition) predict densities from 10,000 kg/m^3 at the core boundary to 13,000 kg/m^3 at the centre; see, e.g., Fig. 5.25. Silicates cannot be compressed to this density by the pressures expected in the Earth's core.
2. The fluidity and electrical conductivity of the silicates in the Earth's mantle are too low to produce the observed magnetic field of the Earth. The magnetic field is therefore produced by the core. This requires the core to be both liquid and metallic.
3. The seismologically observed density and P-wave velocity (sound speed) in the core are close to those of iron measured in the laboratory at similar temperatures and pressures. (These temperatures and pressures can be produced in the lab in a special device called a diamond-anvil cell.)
4. Cosmically, iron is by far the most abundant element having these properties.

An important insight into core formation in the Earth is provided by the measured Ni/Co (nickel to cobalt) ratio in the mantle. Ni and Co are moderately siderophile and both are depleted in the mantle relative to chondritic composition, as expected. However, at least at low pressures, Ni is more strongly siderophile than Co and should be more depleted, whereas in fact the Ni/Co ratio in the mantle is close to chondritic. The solution to this discrepancy was provided by high-pressure experiments (Li and Agee 1996) which show that both Ni and Co become less siderophile with increasing pressure, and are equally siderophile at ~28 GPa, corresponding to a depth of 750 km in the present Earth. This in turn suggests (Wood 2011) that the iron

in impacting asteroids, in which the cores had formed at low pressure, did not sink directly to the Earth's core, but spent time at an intermediate depth where it had time to re-equilibrate (i.e., reach chemical equilibrium) with the silicate mantle at high pressure before continuing to sink. One possible model that would be consistent with this result is a 750-km deep outer mantle kept molten by impact heating and radiogenic heat from ^{235}U, ^{238}U, ^{232}Th, ^{40}K (see Chap. 6) and short-lived radioactive isotopes such as ^{26}Al ($t_{1/2} = 7.17 \times 10^5$ year). The molten outer mantle would be separated from the molten iron core by a solid inner mantle. An incoming asteroid would melt on impact, and its iron core would sink in droplets through the molten outer mantle and pool at the top of the solid inner mantle, where it would have time to equilibrate with the silicate. When enough of the denser iron had accumulated above the lighter rock in the solid inner mantle, the system would become unstable and the iron would sink as large diapirs through the rock and into the core.

5.4.4.1 The Size of the Earth's Core

The fractions of the Earth taken up by the inner and outer core can be summarized as follows:

	Outer core (%)	Inner core (%)
By volume	15.7	0.7
By mass	30.8	1.7
By number of atoms	15.0	0.8

5.4.4.2 The Molten Outer Core

The state of this core must be molten.

The evidence includes the following:

1. The existence of the Earth's magnetic field, as described above.
2. S-waves do not propagate through the outer core, and are not seen.
3. Results from analysis of free oscillations of the Earth as a whole.
4. The character of the Earth's nutation (small wobbles in the direction of the Earth's spin axis): if you spin an egg, it behaves differently depending on whether it is hard-boiled (solid) or raw (fluid inside the shell); similarly, the spinning Earth responds differently to gravitational tugs depending on whether it is entirely solid or has a large molten core.
5. Convective and cyclonic motions occur in the fluid outer core, producing the Earth's magnetic field through dynamo action. Speeds appear to be about 10 km/year.

5.4.4.3 Non-Iron Composition of the Core

The observed density of the outer core is 10 ± 2 % less than that expected for pure iron at the outer core's temperature and pressure, and the inner core is 2.5 % less dense than pure iron at the inner core's temperature and pressure. At least one lighter element (possibly more) is therefore mixed in as an impurity. The element or elements involved are not known. Those that have been suggested (in the form of pro and con arguments) are:

1. Sulfur (S)

For:

- S alloys easily with iron, forming sulphides, at both low and high pressures.
- S lowers the melting temperature of the iron alloy compared to pure iron. This favors the formation of the observed solid inner core because, as the core temperature decreases over geological time, pure iron can separate out, solidify, and sink, forming the inner core, while the alloy in the outer core remains molten (Sect. 5.4.4.5).
- Iron sulphides are found in meteorites (0.7 ± 0.5 % by weight of the iron).
- S is depleted in the mantle compared to cosmic abundances. Enhanced sulfur in the core would account for part of this depletion.

Against:

- S in the core cannot explain all of the sulfur depletion in the mantle, even if sulfur makes up the entire light-element content of the core. At least some sulfur therefore must have been lost to space as a volatile during the formation of the Earth. (The case for sulfur in the core would be strengthened if none could have been lost to space, because then the only place the "missing" mantle sulfur could have gone would be to the core.)
- If sulfur makes up a significant fraction of the light-element content of the core, then it would in fact be more abundant in the Earth as a whole than some elements which are less volatile (less easily lost to space) than sulfur.

2. Oxygen (O)

For:

- Is definitely present, because chemical reactions at the core–mantle boundary necessarily add oxygen to the core. This oxygen will be mixed through the core by convection. (The question is, is it present in significant amounts?)
- Is abundant in the Earth (58 ± 2 % of the mantle by number of atoms).
- FeO becomes metallic at the high pressures found in the Earth's core, and therefore alloys easily with the molten iron there.

Against:

- Does not easily alloy with iron at low pressures. It could therefore not have alloyed with iron until well after the core had begun to form, and perhaps not until after the accretion of the Earth was complete. This may leave chemical reactions at the core boundary as the major source of oxygen in the core, and this may not be significant.

3. Silicon (Si) and Magnesium (Mg)

For:

- Necessarily added by chemical reactions at the core–mantle boundary, as with oxygen.
- Si and Mg relatively abundant (18 $\pm$ 7 % of the mantle by number of atoms).

Against:

- Smaller amounts available compared to oxygen.
- Si and Mg appear to be less reactive with molten iron than oxygen.

4. Hydrogen (H):

For:

- H is abundant in the universe, and also possibly at the Earth's surface during accretion and core formation.
- H alloys with iron easily at high pressures.

Against:

- Most of the Earth's hydrogen was lost to space; the amount (if any) in the core cannot explain the observed deficit compared to cosmic.
- The presence of H in the core seems to require the Earth to remain cold during accretion and subsequent core formation, to prevent the hydrogen from being lost to space. This is contrary to expectation.

5. Nickel (Ni)

For:

- Ni is present in iron meteorites (8 $\pm$ 7 % by weight).
- Ni is depleted in the mantle by an amount which would be completely accounted for if the core contained about 4 % by weight of nickel.
- Ni alloys easily with iron at both low and high pressures.
- Ni lowers the melting point of the iron alloy compared to pure iron and so favors formation of a solid inner core (as noted above for sulfur).

Against:

- Ni has almost the same density as iron, so it does not affect the need for light elements discussed above. In fact, there is *no* geophysical observation that directly indicates the presence of nickel in the core (or any that excludes it).

Clearly there are many candidates, some more likely than others.

5.4.4.4 The Inner Core

The inner core is apparently solid. There are two main lines of evidence:

1. S-waves appear to propagate through the inner core; this is not possible in a liquid.
2. P-wave velocities in the inner core are systematically higher parallel to the Earth's rotational axis (the polar or N–S direction) than parallel to the plane of the equator (Calvet et al. 2006 and references therein). A similar anisotropy is found in the uppermost part of the mantle and is caused by olivine crystals having a preferred direction of orientation (produced by shear associated with convection and plate tectonics). The same mechanism could operate in the inner core if it is also tectonically active (solid but with plastic flow), because solid iron is expected to have a hexagonally close-packed (hcp) crystal structure at the inner core's temperature and pressure, and hcp iron (or ε-Fe) is known to have anisotropic elastic properties.

Because of the high thermal conductivity of solid iron, the inner core is expected to approach isothermality on a timescale of the order of 10^9 years (Williams et al. 1987 and references therein). An age for the inner core can be derived from the fact that it is believed to play a significant role in the production of the Earth's magnetic field, and paleomagnetic measurements show a strong terrestrial magnetic field for at least the past 2.5–3.5 billion years. Although this may be insufficient time to achieve full isothermality, measured data suggest a maximum temperature difference between the center and the inner core boundary of 300 K or less, or about 10 % or less of the temperature difference across the outer core.

5.4.4.5 Formation of the Inner Core

If two substances (e.g., iron and sulfur) are miscible in the liquid phase but, because they have different crystal structures, are immiscible in the solid phase, the result is a *binary eutectic system*. Figure 5.21 illustrates the behavior of such a system, consisting of components A and B. (In the case of iron and sulfur, the two components of the binary system are Fe and FeS.)

If we gradually cool a completely molten mixture that has the eutectic composition (see Fig. 5.21 for terminology), then both components remain molten until the eutectic is reached, and both components crystallize simultaneously until the mixture is completely solid. Such a composition is called a *eutectic mix*. In this case, the system has a well-defined freezing (or melting) temperature, the *eutectic temperature*. However, if the initial composition is to the left of the eutectic in Fig. 5.21 (an example is shown by the thick arrows), then when the melt reaches the liquidus, A begins crystallizing while B and the remainder of A remain molten. As A is removed from the melt, the melt gradually becomes richer in B, so as the temperature continues to decrease, the melt "slides" along the liquidus toward

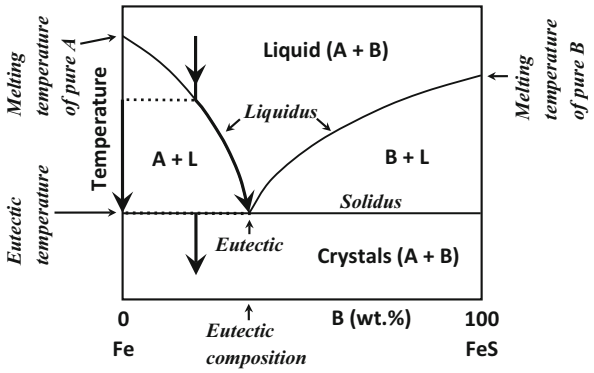

Fig. 5.21 Binary eutectic phase diagram for two components, A and B, that are miscible in the liquid phase and immiscible in the solid phase. The symbol L = liquid. The liquidus curves are the lines above which the entire system is liquid, and the solidus is the line below which the entire system is solid (a mixture of crystals of A and B). In the regions between the liquidus and the solidus, the mixture consists of crystals of one component within a liquid of both components. The eutectic is the point at which all three phases (A, B, and the melt) can exist simultaneously. The thick arrows show an example of cooling a melt that has an initial composition different from the eutectic composition

the eutectic as crystals of pure A continue to form. If the initial composition is to the right of the eutectic, then B crystallizes and the remaining melt slides to the left along the liquidus. In either case, when the melt reaches the eutectic, all of B and the remainder of A crystallize simultaneously until the mixture is completely solid. Eutectic mixes are considered in the contexts of the Moon's and Mercury's interiors in Sects. 8.5.3 and 9.1.4, respectively, and of Europa's and Titan's compositions in Milone and Wilson (2014), Sects. 13.1.2.2 and 13.1.3.1, respectively.

We now need to consider two different cases:

1. *Equilibrium crystallization*: If the crystals remain suspended (e.g., if the liquid is turbulently convective), then the total composition of crystals + melt remains constant. When the melt reaches the eutectic, both B and the remainder of A crystallize simultaneously in a ratio equal to the eutectic composition, but the resulting solid (a mixture of all crystals) has the same composition as the original melt.
2. *Fractional crystallization*: If the crystals sink to form a cumulate pile at the base of the melt and/or rise to form a crust, then they are removed from the melt. The final melt then crystallizes to form a solid with the eutectic composition. The result is that the originally-molten region has become differentiated into (depending on circumstances) perhaps three regions of different composition: a cumulate pile, a solidified final melt with the eutectic composition, and a crust. Depending on the initial melt and the minerals precipitating from it, the cumulate pile and crust can each be chemically differentiated as well (see Sect. 8.6 for an example).

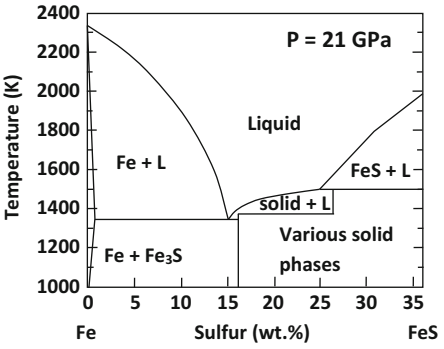

Fig. 5.22 Binary eutectic phase diagram for Fe-S at 21 GPa pressure. The solidus is complicated by the existence of different compounds of Fe + S, including Fe_3S (shown) and Fe_2S. After Fei et al. (2000) with permission from the author and the Mineralogical Society of America. The symbol L = liquid

In the molten iron core of a terrestrial planet, if we take sulfur as the impurity, we can define Fe as component A and FeS as component B. The fraction of FeS (or S) is expected to be below the eutectic composition, so as the core cools, crystals of pure iron begin to form when the system reaches the liquidus (Fig. 5.22). Iron is denser than the melt, so the crystals sink, creating a solid inner core of pure iron surrounded by a molten Fe-FeS outer core. As the planet cools, the solid inner core grows as iron continues to precipitate, and the molten outer core becomes increasingly enriched in sulfur. When the system reaches the eutectic, both Fe and Fe_3S precipitate until the mixture is entirely solid.

Figure 5.23, adapted from Chudinovskikh and Boehler (2007), shows the eutectic composition of the Fe-S system as a function of pressure to 44 GPa. The break in the curve appears to arise because Fe and FeS form a simple binary eutectic system up to 10 GPa (Kamada et al. 2010), but a binary system with intermediate compounds at higher pressures: Fe_3S_2 above 14 GPa and Fe_2S and Fe_3S above 21 GPa. The eutectic composition appears to approach 10 wt% S (*read:* 10 % S by weight) asymptotically as pressure increases above ~40 GPa, which provides an upper limit to the sulfur content of the outer core if the precipitate is to be iron.

The fact that the inner core is 2.5 % less dense than pure iron under inner-core conditions requires that a light element be present in the inner core also. If the light element is sulfur, the required amount is 2.2–6.2 at.% (*read:* 2.2–6.2 % by number of atoms). The hcp phase of iron (ε-Fe) can contain >7.5 at.% (or 4.4 wt.%) S under inner-core conditions, so ε-Fe may be the only iron phase present; or, the inner core could contain a small fraction of Fe_3S (Kamada et al. 2010).

The melting temperature, T_M, of the core material as a function of pressure (and therefore of radius in the Earth) provides a lower limit to the geotherm, T_r, in the molten, outer core and an upper limit in the solid, inner core, and equals T_r at the inner core–outer core boundary (IOB). Thus, T_M provides an important constraint on the geotherm. However, experimental and theoretical uncertainties make T_M uncertain, as do uncertainties in the composition of the core material (Sect. 5.4.4.3); see Boehler (2000) for a review.

Static measurements of T_M in laser-heated diamond-anvil cells have been conducted for pure Fe up to pressures as high as 2 Mbar and in shock-heated

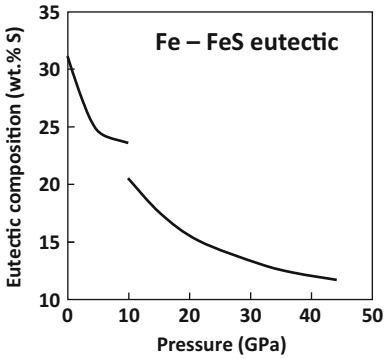

Fig. 5.23 Measured eutectic composition *vs.* pressure for Fe-FeS. See text for details. Adapted with permission from Chudinovskikh and Boehler (2007), and Elsevier, publisher of Earth and Planetary Science Letters

diamond-anvil cells up to about 4 Mbar, and to lower pressures for Fe–FeS systems including Fe_2S and Fe_3S, and for Fe–FeO systems. For comparison, the pressure is about 1.36 Mbar at the core-mantle boundary (CMB) and 3.30 Mbar at the IOB. Shock heating measurements are generally considered less accurate than static measurements because of various uncertainties, including the optical and thermal behaviors of the window material during the shock (Boehler 2000), but provide important constraints on the melting curves.

Several static diamond-anvil studies (Boehler 2000 and references therein) agree on T_M for pure iron in the range 3,100–3,400 K at the CMB, and, by extrapolation to higher pressures, 4,200–5,000 K at the IOB (Fig. 5 of Boehler 2000). As noted above, the presence of S or both S and O can lower T_M by a few hundred K. (Earlier studies indicated that FeO had a higher T_M than pure Fe, but more recent results suggest that, at core pressures, T_M is essentially the same for both FeO and Fe.) With T_M below 5,000 K at the IOB, and assuming temperature changes adiabatically throughout the outer core, T_r on the core side of the CMB is below 4,000 K.

The P- and S-wave speeds and the density as a function of radius are shown for the mantle in Fig. 5.24 and for the entire planet in Fig. 5.25. Finally, the march of pressure, gravitational acceleration, and density through the Earth for the preliminary reference model are plotted in Fig. 5.26.

Some recent analyses of deep-Earth seismic data (Ishii and Dziewonski 2002, 2003; Beghein and Trampert 2003; Calvet et al. 2006; Sun and Song 2008) suggest that the anisotropy of the inner core displays a marked change in character in its innermost part ($r < 300$–450 km, or ~590 km (Sun and Song 2008)). Although several different studies agree on the existence of this innermost inner core, its character remains uncertain. Ishii and Dziewonski (2003), from inverting travel-time data for P-waves and using a ray approximation, find that the fast axis in the innermost inner core could be tilted as much as 55° from the Earth's rotation axis. Even assuming that the fast axis is parallel to the Earth's rotation axis, as it is in the outer part of the inner core, they still find a distinct innermost inner core in that the anisotropy is noticeably stronger. Whether the anisotropy change occurs sharply at a boundary or gradually over a range of radii is unclear. Beghein and Trampert (2003) find the fast axis in the Earth's equatorial plane for P-waves and parallel to the Earth's

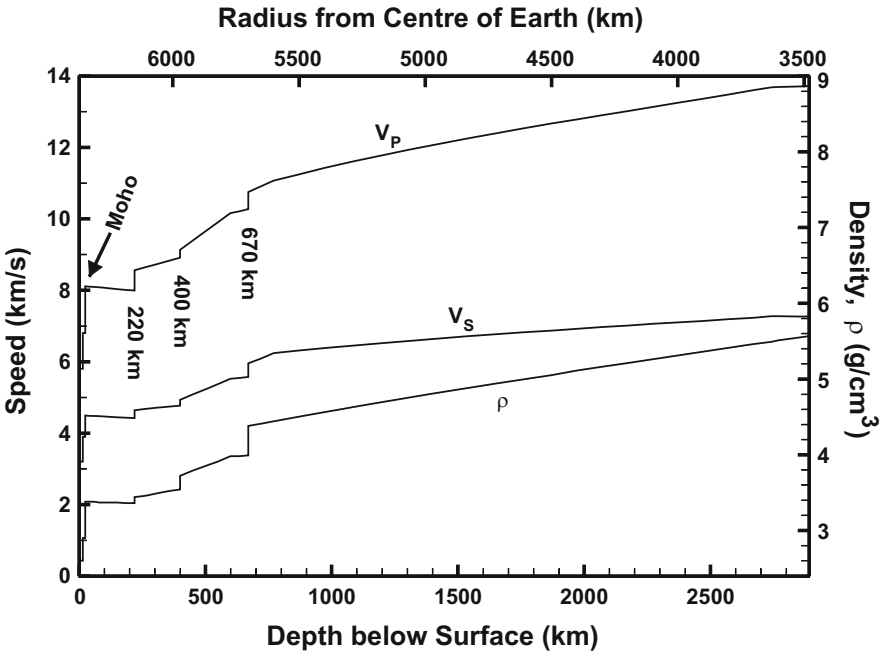

Fig. 5.24 The variation of P- and S-waves and the density through the crust and the mantle. Note the trend for all three quantities to increase with depth. Produced from data published by Dziewonski and Anderson (1981), Table II

rotation axis for S-waves. Calvet et al. (2006) perform an extensive analysis of P-wave data using a more thorough method than previous investigators. Their results agree with previous models for the outer part of the inner core, but for the innermost inner core the data are consistent with any of three basic models: (1) a weak anisotropy with the fast axis in the equatorial plane; (2) near isotropy; and (3) a strong anisotropy with the fast axis parallel to the Earth's rotation axis. In all three cases, the innermost inner core appears distinct in its properties from the outer part of the inner core, despite the lack of constraint on these properties.

This innermost inner core (IMIC) could arise through one of at least three scenarios (Ishii and Dziewonski 2002):

1. The IMIC could be a fossil from an early period of rapid differentiation of the Earth, with the rest of the inner core forming slowly later; in this case, the IMIC could be chemically distinct from the rest of the inner core.
2. The inner core affects the flow pattern in the outer core, and this flow pattern could have changed character when the inner core reached a certain size, altering the anisotropy of the iron core thereafter.
3. The different anisotropy could indicate a different phase of iron at the pressure and temperature of the IMIC.

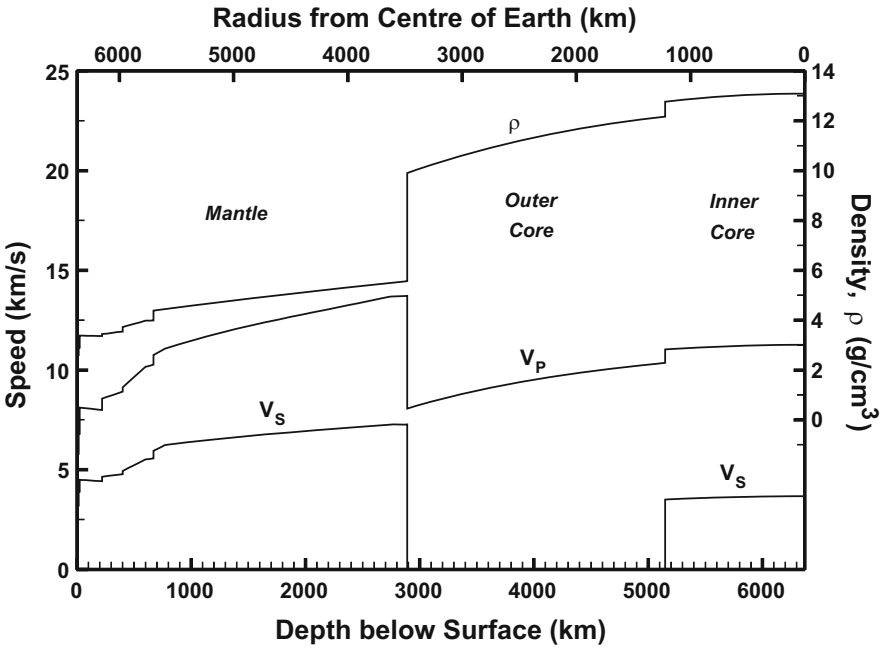

Fig. 5.25 As per Figure 5.24 but for the entire planet. Note the sudden decrease in both P and S velocities at the boundary between the core and the mantle, and the absence of S-waves in the outer core. Produced from data in Dziewonski and Anderson (1981, Table II)

After we discuss the heat flow and internal temperatures (Chap. 6) and the nature of the material in the interior of the Earth (Chap. 7), we will revisit the structure of the Earth and, later, the other terrestrial planets.

5.5 Planetary Surfaces

5.5.1 Impacts

The properties of the surfaces of the rocks reveal something of the history of the planet, especially when that surface has been unmodified for eons—like the surfaces of the Moon or Mercury. The extensive cratering on these surfaces shows the effect of a long period of intense bombardment, which the Earth, Venus, and Mars certainly did not avoid, and may have been more intense for them because of their greater gravitational attraction. The population of small colliders that we know as meteoroids ablates in the atmospheres of the Earth or Venus, but much larger objects—meters or larger in diameter—explosively dissipate much or all of their

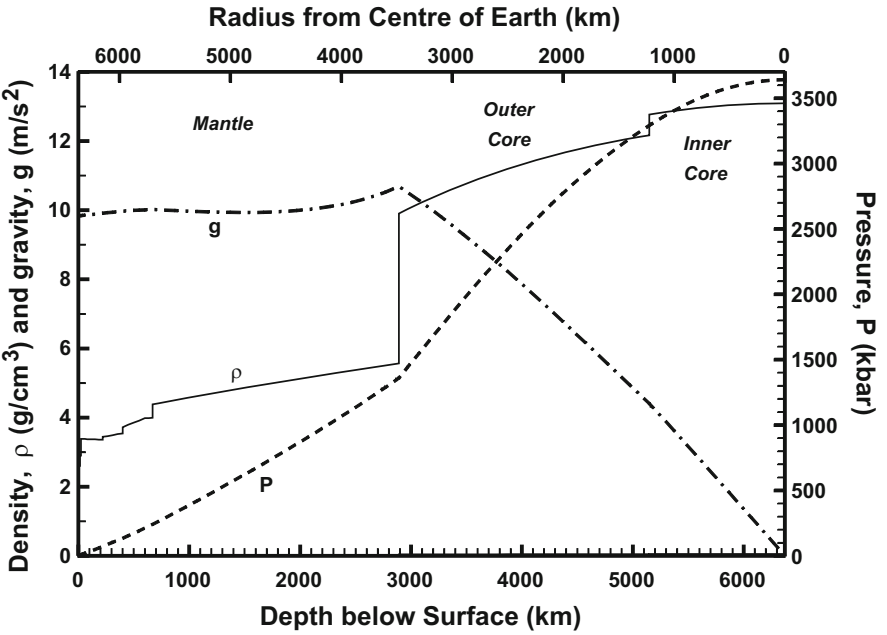

Fig. 5.26 The variation of density, pressure, and gravitational acceleration with radius and depth, according to the preliminary reference Earth model. Produced from data in Dziewonski and Anderson (1981, p. 27)

material. The energy per unit mass arises ultimately from the gravitational potential of the target body but more directly from the relative speed at impact:

$$E = v^2/2 \tag{5.38}$$

The surfaces of Venus, Earth, and Mars have shown significant modification since a period of intense bombardment in the solar system, some 4 Gy ago.

In the case of Mars, as we shall see, the modification has been selective; on Earth and Venus it has been extensive.

The effect of an impact depends critically on the velocity of the impact and the mass of the impactor. The mass of a meteoroid is unknown typically, but if its size can be determined, an estimate of its density leads to a mass. The density ranges from 1,000 kg/m^3 for a "rubble pile" asteroid (an aggregation of loosely packed material) to solid nickel–iron, ~8,000 kg/m^3. The speed of impact depends on the orbit of the impactor. If a meteoroid is initially traveling in a parallel path to the planet and has in effect no net speed with respect to it, the meteoroid will fall to the planet's surface with the escape velocity of that planet:

$$v_{\mathrm{esc}} = \left[2GM_{\mathrm{p}}/R_{\mathrm{p}}\right]^{\frac{1}{2}} \tag{5.39}$$

This quantity is 11.2 km/s for the Earth and only 5.01 km/s for Mars. A meteoroid of asteroidal origin is likely to have originated in the asteroid belt between Mars and Jupiter, although there is a relatively small population of objects even within the orbit of the Earth. There is also a considerable population of objects in the outer solar system, the "trans-Neptunian objects," which are more or less coplanar to the planets and travel in CCW orbits. These include the icy bodies of the Edgeworth-Kuiper Belt. Finally, far beyond the 100 or so au of this region is the spherically distributed Oort Cloud, from which we get the long-period comets. A cometary object with a semi-major axis, a, of 10,000 au and perihelion distance, q, of 1 au has an eccentricity (cf. Sects. 2.2 and 3.2):

$$e = 1 - q/a = 1 - 10^{-4} \approx 1 \tag{5.40}$$

The speed of an Oort cloud comet at perihelion is therefore just short of the escape velocity from 1 au. This escape speed is:

$$v_{esc} = [2GM_{\odot}/q]^{\frac{1}{2}} = 4.21 \times 10^{4}\mathrm{m/s} = 42.1\ \ \mathrm{km/s} \tag{5.41}$$

It is instructive to compute the speed of impact and the energy released if such a comet with perihelion at 1 au were to encounter the Earth. The important quantity to compute first is the speed of the comet relative to the Earth just before impact. This speed is greatest if the comet is in a retrograde orbit and encounters the Earth in a head-on collision, and least if the comet is in a prograde orbit and catches up to the Earth from behind.

The impact speed may be computed in two steps: (1) find the relative speed, v_1, of the comet and Earth if the Earth did not attract the comet gravitationally; and (2) use conservation of mechanical energy to compute the actual speed, v_2, after the comet falls from infinity (with initial speed v_1) to the surface of the Earth at $r = R_E$.

Step 1: This is a relative motion problem. The perihelion speed of the comet is 42.1 km/s and the Earth's orbital speed (assuming a circular orbit) is 29.8 km/s. If the comet and the Earth are meeting head-on then the relative speed is $v_{1,\max}$ = 42.1 km/s + 29.8 km/s = 71.9 km/s, and if the comet catches up from behind then $v_{1,\min}$ = 42.1 km/s—29.8 km/s = 12.3 km/s.

Step 2: Conservation of mechanical energy:

$$K + U = \text{constant, where } K = \frac{1}{2}m_{comet}v^2 \text{ and } U = -\frac{GM_{Earth}m_{comet}}{r}$$

U = 0 at r = ∞, so

$$\frac{1}{2}\mathrm{m}_{comet}v_2^2 \; - \frac{GM_{Earth}m_{comet}}{R_E} = \frac{1}{2}m_{comet}v_1^2 - 0$$

Solving for v_2,

$$v_2^2 \; = v_1^2 + \frac{2GM_{Earth}}{R_E}$$

where, by (5.41), the second term on the right is the square of the Earth's escape speed. Then

$$v_{2,\min} = \sqrt{v_{1,\min}^2 + v_{esc}^2} = \sqrt{(12.3\ \text{km/s})^2 + (11.2\ \text{km/s})^2} = 16.6\ \text{km/s}$$

$$v_{2,\max} = \sqrt{v_{1,\max}^2 + v_{esc}^2} = \sqrt{(71.9\ \text{km/s})^2 + (11.2\ \text{km/s})^2} = 72.8\ \text{km/s}$$

The energy per unit mass involved in such a collision would be, from (5.38),

$$E_{\min} = \tfrac{1}{2}v_{2,\min}^2 = \frac{1}{2}\left(1.66 \times 10^4\ \text{m/s}\right)^2 = 1.38 \times 10^8\ \text{J/kg}$$

$$E_{\max} = \tfrac{1}{2}v_{2,\max}^2 = \frac{1}{2}\left(7.28 \times 10^4\ \text{m/s}\right)^2 = 2.65 \times 10^9\ \text{J/kg}$$

for Earth impact. Because the chemical energy released in a TNT explosion is 4.2×10^6 J/kg, the maximum energy released in a head-on cometary collision would be equivalent to ~630 kg of TNT per kg of impactor mass. Small impactors (meters across or less) ablate as they are passing through a planetary atmosphere, and fragments fall to the surface at the terminal velocity, not the escape velocity. Large objects (hundreds of meters to tens of kms), on the other hand, will not be slowed down very much and will impact with great violence, resulting in a very large crater and substantial deposition of material from the conical sheet that is excavated by the impact over the rim and at the center. The material at the forward edge and at ground zero will be vaporized by the high temperatures resulting from the transfer of kinetic energy; the high vapor pressure will then cause a recoil on the trailing edge of the material, which may break up and become distributed over a wide area or even be re-ejected.

In a planetary atmosphere, the material may be carried around the planet, eventually falling to the surface.

O'Keefe and Ahrens (1986) demonstrated that oblique impacts across a limited range of impact angles and speeds would be able to cause ejection of lightly shocked surface material through entrainment of the ejecta plume. Their Fig. 3 indicates that fragments between 10 cm and 100 cm can be ejected by a low-density impactor with a diameter between 1 and 100 m. This can account,

e.g., for the SNC meteorites (Milone and Wilson 2014, Sect. 15.3.2). The relevant equation is

$$r_p = \frac{3\rho_g x}{2\rho_p} \tag{5.42}$$

where r_p and ρ_p are the plume-entrained fragment radius and density, respectively, ρ_g is the density of the high-velocity plume, and x is a plume radius.

A recent event demonstrated that meteoritic impacts are not merely of academic interest, but a clear and present danger! On February 15, 2013, an airburst near the Russian city of Chelyabinsk (about 300 km west of Tunguska, site of an even larger airburst in 1908) blew the glass out of windows and damaged many buildings, injuring 1,500 people. The meteoroid had entered the atmosphere over a region bordering four countries: Mongolia, China, Russia and Kazakhstan, at an angle of approach of ~16° and proceeding WNW, disintegrated at an altitude of ~23 km. From the brightness of the fireball (V = –28, 3× brighter than the Sun) the estimated diameter of the impacting object was ~ 17 m, its mass, ~ 1.1×10^7 kg, and the energy of the explosion equivalent to ~440 kt or 4.4×10^8 kg of TNT (Durda 2013). The Tunguska event measured 3–5 megatons.

We will discuss the roles played by impacts on the surfaces of the planets and moons of the solar system in later chapters (Chap. 8 for the Moon, Chap. 9 for the surfaces of the individual terrestrial planets, and Milone and Wilson (2014, Chap. 13) for the other moons of the solar system).

5.5.2 Observing Planetary Surfaces

5.5.2.1 Phase and Visibility

The *phase, q,* of a planet is the fraction of a planet's diameter that appears illuminated by the Sun as viewed from the Earth (or any other platform from which you are viewing the planet!—for now we assume that the Earth is the only viewing site).

The *phase angle, ϕ,* is the angle at the center of the planet between the directions to the Sun and to the Earth. The relation between q and ϕ is:

$$q = \frac{1}{2}(1 + \cos\phi) \tag{5.43}$$

See Fig. 5.27 for the geometry needed to derive this equation.

Note that when $\phi = 0°$, the planet is fully illuminated (this is a possible configuration for all planets but for practical reasons only an exterior planet can be well viewed when fully illuminated, which for those planets occurs at opposition).

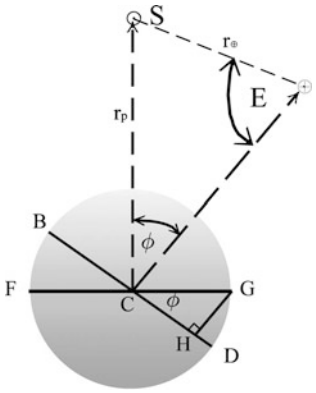

Fig. 5.27 Definition of phase angle

When $\phi = 90°$, half the planet appears illuminated. At a phase angle of 180°, $q = 0$. This is the case only at inferior conjunction, and is possible only for an interior planet.[6]

Although all phase angles are possible for an interior planet (whether easily viewable or not!), this is not true for exterior planets. In those cases, $0° \leq p < 90°$, but even sharper constraints can be found, so that p_{max} and q_{min} may be specified for a given planet.

The sine law for plane triangles allows the phase angle of a planet to be calculated from the *elongation, E* (the angle between the Sun and the planet measured at the Earth, $\sphericalangle S_{\oplus} C$ in Fig. 2.4), and the distances of the Earth from the Sun, r_0, and of the Sun from the planet, r_p, respectively, at any instant.

$$\sin \phi / r_{\oplus} = \sin E / r_p \tag{5.44}$$

From (5.44), for given values of $r_{\oplus}$ and r_p, the maximum phase angle, ϕ_{max} (and therefore minimum phase, q_{min}) of a superior planet occur at *quadrature* ($E = 90°$);

$$\sin \phi_{max} = r_{\oplus} / r_p \tag{5.45}$$

From (5.44) and (5.45), for superior planets, $\phi_{max} \rightarrow 90°$ only if $r_p \rightarrow r_{\oplus}$. Mars has the smallest orbit beyond the Earth's and therefore attains the maximum departure from full phase that we see among the superior planets. The maximum possible value of ϕ_{max} for Mars occurs on the extremely rare occasion when the

[6] *Interior*, that is, to the Earth's orbit. Classically, Mercury and Venus are "inferior planets," because they orbit below the orbit of the Sun in the Ptolemaic, geocentric universe. Similarly, planets *exterior* to the Earth's orbit, Mars on out, were classically referred to as "superior planets," because their orbits lay above that of the Sun. In modern usage, "inferior" and "superior" have acquired heliocentric meanings and are used interchangeably with "interior" and "exterior" respectively. See Chapter 1 and Kelley and Milone (2011) for details, configurations, and terminology.

Earth is at aphelion at the same instant that Mars at *quadrature* ($E = 90°$) is at perihelion. From (5.45),

$$\phi_{\max} = \arcsin(1.017/1.381) = 47.^{\circ}4$$

which, when inserted in (5.43), leads to a minimum possible phase, $q_{\min} = 0.838$. Because of the low probability of the required conditions occurring, observed phases of Mars will almost always be greater than this.

5.6 Addendum: Properties of Legendre Polynomials and Associated Legendre Functions

In simpler form, the function of interest in (5.7), namely,

$$\begin{aligned}\sum_{n=0}^{\infty} P_n(\cos\theta)\left(\frac{a}{r}\right)^n &= \left[1 - 2(\cos\theta)\left(\frac{a}{r}\right) + \left(\frac{a}{r}\right)^2\right]^{-1/2} \\ &= \sum_{n=0}^{\infty} \frac{(2n)!}{2^{2n}(n!)^2}\left[2(\cos\theta)\left(\frac{a}{r}\right) - \left(\frac{a}{r}\right)^2\right]^n\end{aligned} \tag{5.46}$$

is convergent for $(a/r) < 1$. The *Legendre polynomial* part of this function, $P_n(\cos\theta)$, is written as;

$$P_n(x) = \sum_{k=0}^{[n/2]} (-1)^k \frac{(2n-2k)!}{2^n\, k!(n-k)!(n-2k)!} x^{n-2k} \tag{5.47}$$

where $x \equiv \cos\theta$, and the upper limit on the summation $[n/2] = n/2$ for even, and (n − 1)/2 for odd, n. Whence, $P_0(x) = 1, P_1(x) = x, P_2(x) = \frac{3}{2}x^2 - \frac{1}{2} = \frac{1}{2}(3x^2 - 1)$, $P_3(x) = \frac{1}{2}(5x^3 - 3x)$, and, generally,

$(2n + 1)xP_n(x) = (n + 1)P_{n+1}(x) + nP_{n-1}(x)$, $n = 1, 2, 3, \ldots$, Also
$\partial P_{n+1}/\partial x = (n + 1)P_n(x) + x\partial P_n(x)/\partial x$.

Further, we can write,

$$P_n(x) = \frac{1}{2^n\, n!} = \left(\frac{\mathrm{d}^n}{\mathrm{d}x^n}\right)\left(x^2 - 1\right)^n \tag{5.48}$$

Finally, where "m = 0/1" designates "either 0 or 1," $P_n(x)$ can be written

$$P_n(\cos\theta) = \sum_{m=0/1}^{n} a_m \cos m\theta = \sum_{m=0/1}^{n} a_m \left(e^{im\theta} + e^{-im\theta}\right) \tag{5.49}$$

The *Associated Legendre functions* are characterized by:

$$P_n^m(x) = \left(1 - x^2\right)^{m/2} \left(\frac{d^m}{dx^m}\right) P_n(x) \tag{5.50}$$

where $m \leq n$. Thus, $P_1{}^1(x) = (1 - x^2)^{1/2} = \sin\theta$; $P_2{}^1(x) = 3x(1 - x^2)^{1/2} = 3\cos\theta \sin\theta$, $P_2{}^2(x) = 3\sin^2\theta$, ...

Challenges

[5.1] Derive equation (5.3b) in footnote 3.

[5.2] Assume that a meteoroid originates from a direct orbit with $a = 1.333$ au and $e = 0.25$, and collides with the Earth. Compute its speed at 1 au and on impact with Earth. If the object has a diameter of 100 m and a mean density of 3,300 kg/m^3, compute (a) the energy per unit mass and (b) the total energy of the explosion. (c) What do you suppose will happen if the object strikes an ocean rather than land? Will it leave a crater, for instance?

[5.3] Derive equation (5.34) and demonstrate why an exterior planet cannot be observed at phase angles $\leq 90°$. Show also that the maximum observed phase angle for an exterior planet occurs when the planet is at quadrature.

[5.4] Prove that the phase is a minimum when the phase angle is a maximum. Compute the minimum observable phases for the asteroid Ceres, Jupiter, and Pluto. (Orbital data are available in Milone and Wilson (2014), Chaps. 15, 12, and 13, respectively.)

[5.5] From the data and relations given in Sect. 5.5.1, calculate the speed at which the Chelyabinsk meteor exploded.

[5.6] Derive the equation of hydrostatic equilibrium (5.17), from the basic definition of the pressure on a cylinder of gas of cross-sectional area A and height h, subject to a gravitational acceleration g in a gas of density ρ.

References

Beghein, C., Trampert, J.: Robust normal mode constraints on inner-core anisotropy from model space search. Science **299**, 552–555 (2003)

Boehler, R.: High-pressure experiments and the phase diagram of lower mantle and core materials. Rev. Geophys. **38**, 221–245 (2000)

Calvet, M., Chevrot, S., Souriau, A.: P-wave propagation in transversely isotropic media II. Application to inner core anisotropy: effects of data averaging, parametrization and a priori information. Phys. Earth Planet. Inter. **156**, 21–40 (2006)

Chudinovskikh, L., Boehler, R.: Eutectic melting in the system Fe–S to 44 GPa. Earth Planet. Sci. Lett. **257**, 97–103 (2007)
Consolmagno, G.J., Schaefer, M.W.: *Worlds Apart: A Textbook in Planetary Sciences*. Prentice Hall, London (1994)
Deschamps, F., Kaminski, E., Tackley, P.: A deep mantle origin for the primitive signature of ocean island basalt. Nat. Geosci. **4**, 879–882 (2011)
Durda, D.: The Chelyabinsk super-meteor. Sky Telesc **125**(June), 24–31 (2013)
Dziewonski, A.M., Anderson, D.L.: Preliminary reference earth model. Phys. Earth Planet. Inter. **25**, 297–356 (1981)
Fei, Y., Li, J., Bertka, C.M., Prewitt, C.T.: Structure type and bulk modulus of Fe3S, a new iron-sulfur compound. Am. Mineral. **85**, 1830–1833 (2000)
Fortney, J.J.: The structure of Jupiter, Saturn, and exoplanets: key questions for high-pressure experiments. Astrophys Space Sci **307**, 279–283 (2007)
Gutenberg, B; Richter, C. F.: Magnitude and energy of earthquakes. Science **83** (2147), 183–185 (1936)
Henning, W.G., O'Connell, R.J., Sasselov, D.D.: Tidally heated terrestrial planets: viscoelastic response models. Astrophys J **707**, 1000 (2009)
Hunter, G.W., Ponchak, G.E., Dyson, R.W., Beheim, G.M., Scardelletti, M.C., Meredith, R.D., Taylor, B., Kiefer, W. S. Development of a High Temperature Venus Seismometer and Extreme Environment Testing Chamber. International Workshop on Instrumentation for Planetary Missions, Greenbelt, Maryland. Abstract 1133 (2012)
Ishii, M., Dziewonski, A.: The innermost inner core of the earth: evidence for a change in anosotropic behavior at the radius of about 300 km. Proc. Natl. Acad. Sci. U. S. A. **99**, 14026–14030 (2002)
Ishii, M., Dziewonski, A.: Distinct seismic anisotropy at the centre of the earth. Phys. Earth Planet. Inter. **140**, 203–217 (2003)
Islam, M.A., Ebihara, M., Kojima, H. Chemical Compositions and Alteration of Primitive Carbonaceous Chondrites. 43rd Lunar and Planetary Science Conference, abstract 1974 (2012)
Kamada, S., Terasaki, H., Ohtani, E., Sakai, T., Kikegawa, T., Ohishi, Y., Hirao, N., Sata, N., Kondo, T.: Phase relationships of the Fe-FeS system in conditions up to the Earth's outer core. Earth Planet. Sci. Lett. **294**, 94–100 (2010)
Kelley, D.H., Milone, E.F.: *Exploring Ancient Skies*, 2nd edn. Springer, New York (2011)
Ksanfomaliti, L.V., Zubkova, V.M., Morozov, M.A., Petrova, E.V.: Microseisms at the *Venera 13* and *Venera 14* landing sites. Pis'ma Astronomicheskii Zhurnal **8**, 444–447 (1982)
Li, J., Agee, C.B.: Geochemistry of mantle-core differentiation at high pressure. Nature **381**, 686–689 (1996)
Lorenz, R.D., Nakamura, Y. Viking Seismometer Record: Data Restoration and Dust Devil Search. 44th Lunar and Planetary Sciences Conference, abstract 1178 (2013)
Love, A.E.H.: Some Problems of Geodynamics. Cambridge University Press, Cambridge (1911)
Milone, E.F., Wilson, W.J.F.: Solar System Astrophysics: Planetary Atmospheres and the Outer Solar System, 2nd edn. Springer, New York (2014)
O'Keefe, J.D., Ahrens, T.J.: Oblique impact: a process for obtaining meteorite samples from other planets. Science **234**, 346–349 (1986)
Richter, C. F.: An instrumental earthquake magnitude scale. Bul. Seismological Soc. of Amer. **25** (1), 1–32 (1935).
Stewart, A., Schmidt, M.W., van Westrenen, W., Liebske, C.: Mars: a New core-crystallization regime. Science **316**, 1323–1325 (2007)
Sun, X., Song, X.: The inner inner core of the earth: texturing of iron crystals from three-dimensional seismic anisotropy. Earth Planet. Sci. Lett. **269**, 56–65 (2008)
Tromp, J.: Inner-core anisotropy and rotation. Annu. Rev. Earth Planet. Sci. **29**, 47–69 (2001)
Williams, Q., Jeanloz, R., Bass, J., Svendsen, B., Ahrens, T.J.: The melting curve of iron to 250 GPa: a constraint on the temperature at the Earth's center. Science **236**, 181–182 (1987)
Wood, B.: The formation and differentiation of earth. Phys Today **64**, 40–45 (2011)